



Article

Does the Catalyst Always Assist the Methylene Blue Photodegradation or does It Sometimes Hinder It? †

Chiara Alessandrello¹, Zainab Dahrouch¹, Salvatore Maida¹, Moreno D'Ambrosio², Salvatore Patanè^{2,3,*}, Saveria Santangelo^{1,3,*} and Claudia Triolo^{1,3}

¹ Dipartimento di Ingegneria Civile, dell'Energia, dell'Ambiente e dei Materiali (DICEAM), Università "Mediterranea", 89122 Reggio Calabria, Italy

² Dipartimento di Scienze Matematiche e Informatiche, Scienze Fisiche e Scienze della Terra (MIFT), Università di Messina, 98166 Messina, Italy

³ National Reference Center for Electrochemical Energy Storage (GISEL), Consorzio Interuniversitario Nazionale per la Scienza e Tecnologia dei Materiali (INSTM), 50121 Firenze, Italy

* Correspondence: salvatore.patane@unime.it (S.P.); saveria.santangelo@unirc.it (S.S.)

† This article is dedicated to Prof. Giuseppe Zerbi in recognition of his outstanding scientific contributions to Spectroscopy.

How To Cite: Alessandrello, C.; Dahrouch, Z.; Maida, S.; et al. A Does the Catalyst Always Assist the Methylene Blue Photodegradation or does It Sometimes Hinder It? *Photochemistry and Spectroscopy* 2026, 2(1), 8. <https://doi.org/10.53941/ps.2026.100008>

Received: 17 November 2025

Revised: 23 December 2025

Accepted: 4 January 2026

Published: 2 March 2026

Abstract: Lattice defects, particularly oxygen vacancies, are commonly considered beneficial to photocatalytic performance, as they can reduce the bandgap, broaden the light absorption range, and suppress electron/hole recombination. In this perspective, high-entropy oxides (HEOs) could be considered "ideal" materials for photocatalysis because the random distribution of multiple metal cations within the crystalline lattice generates intrinsic structural disorder, which can be modulated by varying their composition and synthesis conditions. This work studies the photocatalytic activity of electrospun Cr–Mn–Fe–Co–Ni-based HEOs for the degradation of methylene blue in aqueous solution. The selected preparation conditions (calcination in air at 400 °C for 2 h) yield nanofibers consisting of ultra-small grains (≤ 9 nm) with copious oxygen vacancies on their surface. The presented results raise an important question: does the catalyst always promote the dye photodegradation or does it sometimes hinder it? A critical discussion is proposed, highlighting the case in which defects can induce competitive recombination pathways, negatively impacting the material's photocatalytic performance.

Keywords: high-entropy oxides; defects; oxygen vacancies; grain boundaries; methylene blue; photocatalysts

1. Introduction

The dispersion of methylene blue (MB), 3,7-bis(dimethylamino)phenothiazin-5-ium chloride, represents a significant example of water pollution. MB is an organic compound characterized by strong reducing activity. Owing to this interesting property, it is successfully used in medicine for the treatment of methemoglobinemia. Additionally, this organic compound is also used in analytical chemistry as an indicator in oxidation-reduction reactions, in sulphide analysis, and as a peroxide generator. MB is also used in aquaculture as a bactericidal and antiprotozoal agent and as a dye in biological, textile and food industries [1,2]. Despite the evident beneficial use of MB, the high and uncontrolled release of MB in water represents a serious risk for the ecosystem and human health preservation.

For these reasons, great efforts are devoted to the development of efficient materials for contaminant removal and sustainable water treatment processes. Conventional methods for wastewater purification include [3]: (i) the chlorination, which involves the addition of chlorine to the water; (ii) ozonation, where ozone is introduced to eliminate bacteria and other microorganisms; (iii) adsorption, which employs various materials to adsorb



Copyright: © 2026 by the authors. This is an open access article under the terms and conditions of the Creative Commons Attribution (CC BY) license (<https://creativecommons.org/licenses/by/4.0/>).

Publisher's Note: Scilight stays neutral with regard to jurisdictional claims in published maps and institutional affiliations.

contaminants from water; (iv) membrane technology, which uses selective membranes to separate pollutants; (v) coagulation and flocculation, in which chemicals are added to aggregate fine particles into larger clumps (flocs) that can be removed by filtration; (vi) biological degradation that employs bacteria to disintegrate contaminants in the water. Finally, photocatalytic degradation is an emerging and promising technology for environmental purification, particularly for the decomposition of harmful pollutants. In this process, pollutant molecules are broken down through a photo-activated catalytic reaction facilitated by proper photocatalysts (PCs), such as reduced graphene oxide, multi-walled and single-walled carbon nanotubes, metal-organic frameworks, covalent organic frameworks, biodegradable polymers, and metal oxides [4–8]. Since the photocatalytic reaction primarily involves their surface, nanostructured materials, featured by high surface-to-volume ratio and a greater number of active sites, are often the materials of choice.

Among the metal oxides, extensive research has focused on both binary and ternary oxides, such as TiO₂ [9,10], ZnO [11], SnO₂ [12], ZrO₂ [13], BiVO₄ [14], and SrTiO₃ [15]. Most of these metal oxides possess wide energy gap (E_g) values and therefore require UV light to activate the photocatalytic process. However, since the UV radiation accounts for only about 10% of the solar spectrum, current research in photocatalytic materials aims to develop oxides with narrower band gaps, such as Fe₂O₃ [16] and WO₃ [17], or to properly engineer UV-active oxides through structural defect modification, doping, and morphological control of nanostructures [18]. These strategies are well documented for ZnO, for which the photocatalytic performance can be improved by increasing the elemental impurities in the wurtzite structure. This results in the introduction of electron capture centres that reduce the probability of the electron/hole recombination [11,19].

Since the structural defects play a pivotal role in enhancing the photocatalytic activity and reducing the E_g of metal oxides, high-entropy oxides (HEOs) have emerged as highly promising candidates in this research field. Owing to their “intrinsic crystal disorder”, arising from the random distribution of multiple metal cations within the crystalline lattice, and to the opportunity to easily tune their compositional, optical, magnetic, electrical, and electrochemical properties by varying the metal constituents and the synthesis conditions [20], HEOs can represent the “ideal” materials for photocatalytic pollutant degradation. The intrinsic defects and strain can enhance photocatalytic activity through multiple mechanisms, including bandgap narrowing that broadens the light absorption range and suppression of electron–hole recombination mechanisms [21]. In HEO family, the presence of the oxygen anions in the lattice determines a high selectivity in the crystalline phases that can be formed, i.e., rock-salt, fluorite, perovskite and spinel structures. All these crystalline phases have been tested for their photocatalytic activity.

Jia et al. [22] have investigated the effect of Fe molar ratio in (La_{0.2}Ce_{0.2}Gd_{0.2}Zr_{0.2}Fe_x)O₂ PCs for the degradation of tetracycline hydrochloride. They have reported that the increase in Fe molar concentration favors the decrease of the valence band position and a better crystalline order. The best photodegradation performance is attributed to HEO containing 0.05 molar Fe concentration, which is characterized by appropriate band structure and abundant defects, achieving 95.4% photodegradation of tetracycline hydrochloride under visible illumination within 3 h. Pradhan et al. [23] have proposed (Mn_{0.6}Cr_{0.6}Co_{0.6}Fe_{0.6}Al_{0.6})O₄, produced by the sol-gel method and subsequent calcination in air at 900 °C for 1.5 h, as PC for the degradation of MB. Owing to the generation of electron-hole pair under UV irradiation and the contribution of all constituent metal ions, this HEO shows good performance as PC, favoring a complete degradation of MB in 90 min. In addition, the magnetic properties associated to its inverse-spinel structure are attractive for the PC recovery after pollutant degradation. Zhang et al. [24] have analyzed HEOs based on combinations of five metals among Cr-Mn-Fe-Co-Ni-Cu prepared by the chemical solution deposition method on amorphous quartz substrates. Among them, (Co_{0.2}Mn_{0.2}Fe_{0.2}Cr_{0.2}Cu_{0.2})₃O₄ shows the best photocatalytic effect (up to 8.5 times higher than the remaining HEOs) and spectral response up to the near-infrared region. Du et al. [25] have utilized pyrochlore (La_{0.2}Nd_{0.2}Sm_{0.2}Gd_{0.2}Y_{0.2})₂Zr₂O₇ powders, prepared via the sequence coprecipitation–hydrothermal–calcination method, for the photodegradation of Rhodamine B. Grain size reduction plays in enhancing the photocatalytic activity for the degradation of Rhodamine B solution under UV exposure.

This work focuses on the study of spinel-type Cr-Mn-Fe-Co-Ni-based HEOs as PCs for the MB degradation. HEOs based on this combination of transition metals have already been successfully employed as electrocatalysts for the oxygen evolution reaction (OER) [26–28], demonstrating that defect-engineering and preferential occupation of 16d octahedral sites by the most redox-active species are useful for improving electrocatalytic performance and water splitting kinetics. Cr-Mn-Fe-Co-Ni HEOs have also been successfully used as passive fillers in the preparation of poly(ethylene oxide) (PEO)/lithium bis(trifluoromethanesulfonyl) imide (LiTFSI)-based solid composite electrolytes (SCEs) [29,30]. In this case, proper calcination conditions and rapid quenching allow controlling the density of the surface defects in the fillers, which affects the SCE ionic conductivity.

Given the well-established role of surface defects in catalytic processes, this study focuses on clarifying the relationship between synthesis conditions, surface defect density and photocatalytic activity of electrospun Cr-Mn-Fe-Co-Ni HEOs. Calcination is performed at low temperature (400 °C for 2 h) to produce ultra small HEO grains and is followed by rapid uncontrolled cooling to generate a high density of structural defects on their surface and kinetically trap the metastable crystalline phase formed during the heat treatment [29].

2. Experimental Section

2.1. Synthesis of the Electrospun Photocatalysts

Cr-Mn-Fe-Co-Ni HEOs are synthesized following the procedure described in detail in a previous paper [26]. Briefly, the spinnable solution is prepared by dissolving in a polyacrylonitrile (PAN)/dimethylformamide (DMF) mixture Cr-, Mn-, Fe-, Co-, and Ni-acetates with a double amount of each metal in turn finally obtaining a set of five non-equimolar HEO samples. A CH-01 Electro-spinner 2.0 (Linari Engineering s.r.l.) operating at room temperature (RT) and 40–45% relative air humidity is used for the electrospinning. HEO powders obtained by calcination in air (400 °C for 2 h) are coded as 2X, where X is the metal with doubled concentration. An additional equimolar Cr-Mn-Fe-Co-Ni HEO (eq-HEO) is prepared for comparison purposes by the same synthesis route and calcination in air at 800 °C for 2 h. After calcination, the physicochemical properties of the samples are studied as described below.

2.2. Physicochemical Characterization

The HEO morphology and composition are investigated by transmission electron microscopy (TEM), using FEI Talos F200S scanning/transmission electron microscope (operated at 200 kV and equipped with an EDX spectrometer for elemental mapping). XRD analysis is carried out with a Bruker D2 diffractometer using Ni β -filtered Cu-K α radiation source ($\lambda = 0.1541$ nm). The identification of phases is performed by QUALX software (Institute of Crystallography (IC), National Research Council (CNR), Bari, Italy) [31,32] and the diffractograms are analysed by the Rietveld method using Maud 2.992 software. Micro-Raman spectroscopy (MRS) is employed to investigate the crystalline structural features of the oxide. Measurements are performed using a confocal microscope (NTEGRA—Spectra SPM NT-MDT) operating in reflection mode, equipped with a 100X objective (Mitutoyo, NA = 0.75), enabling analysis of surface areas smaller than 0.6 μm^2 . Spectra are collected at multiple random locations across the sample surface to assess the spatial homogeneity of the oxide. Excitation is provided by a 532 nm solid-state laser, with a power of 250 μW at the sample surface. The scattered signal is directed into a monochromator (MS 350, SOL Instruments (Augsburg, Germany)) and dispersed by a diffraction grating of 1800 lines mm^{-1} . Finally, the Raman signal is detected by a cooled CCD camera (ANDOR iDus). Diffuse reflectance measurements are carried out using an integrating sphere (Thorlabs, model 4P4) coupled to a monochromator (CVI) equipped with a cooled CCD camera (ANDOR iDus) to indirectly estimate the E_g values of the electrospun HEOs.

Photocatalytic activity towards MB degradation is evaluated at RT under ultraviolet (UV) irradiation. The test is carried out using different PC loadings (0.9–2.9 mg) dispersed in 3 mL of 15 μM MB/distilled water solution. Before exposure to light, the solution is magnetically stirred in the dark for 1 h to achieve adsorption/desorption equilibrium between the dye solution and the PC and then centrifuged (1000 rpm, 4 min) to separate the PC particles before performing the zero-time measurement. Subsequently, the suspension is exposed, at given time intervals, under continuous stirring to prevent PC sedimentation. A Xe lamp is used as a light source for the photodegradation, selecting the wavelength (340 nm, power density of 5 mW cm^{-2}) by means of a monochromator (HORIBA Jobin Yvon model H10UV). At the end of each interval, the solution is centrifuged again and the MB photodegradation is monitored by recording UV-Vis absorption spectra at different irradiation times, using a Perkin-Elmer Lambda 2 UV-Vis spectrophotometer. The degradation percentage of MB solution is estimated as $D = 100(1 - A_t/A_0)$, with A_0 and A_t denoting the initial absorbance and absorbance at an irradiation time t .

3. Results and Discussion

3.1. Structural Characterization of HEOs

In line with the results of previous study [28], HRTEM analysis evidences the formation of micrometer-long nanofibers composed of compactly assembled nanograins (Figure 1a–j). The average nanograin size varies slightly with composition but is always less than 10 nm. STEM-EDX mapping confirms the formation of a multicomponent solid solution (Figure 1k–l).

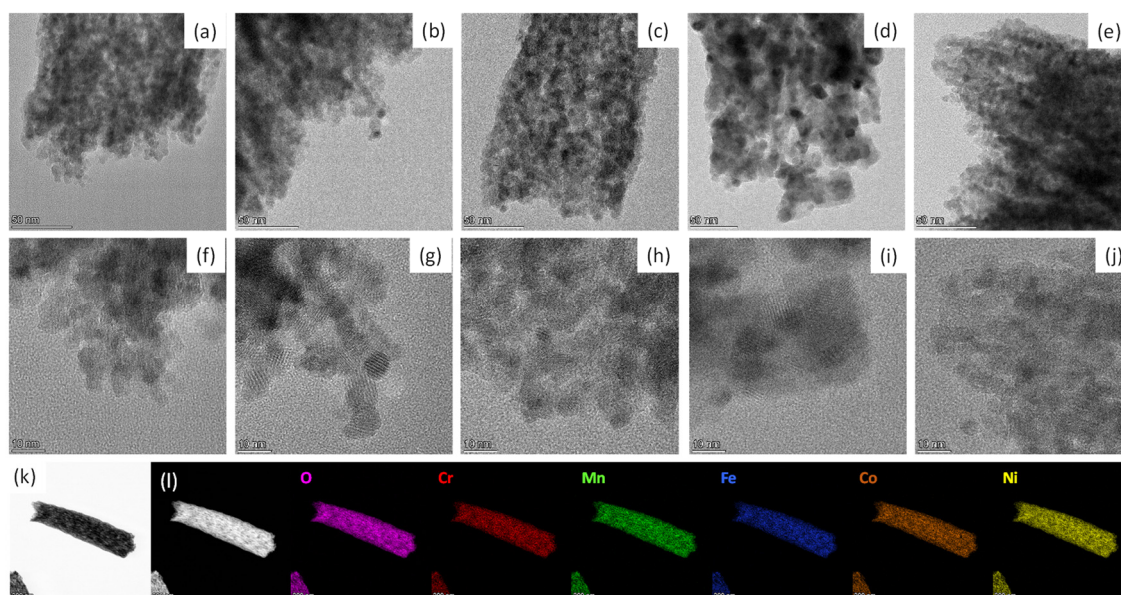


Figure 1. (a–j) HRTEM images of electrospun HEOs: (a,f) 2Cr; (b,g) 2Mn; (c,h) 2Fe; (d,i) 2Co and (e,j) 2Ni. (k) BF-STEM and (l) HAADF-STEM images, followed by the elemental maps. The case of 2Ni is shown.

In agreement with indications emerged from previous studies [28], XRD analysis (Figure 2a) demonstrates the formation of oxides with spinel structure (space group $Fd-3m$), but Rietveld refinements reveal the presence of 10–30 wt% impurities with rock-salt structure (space group $Fm-3m$) in all nanofibers. The average crystal size (5.0–9.2 nm), comparable to the grain size, demonstrates that the fibers are composed of single crystals.

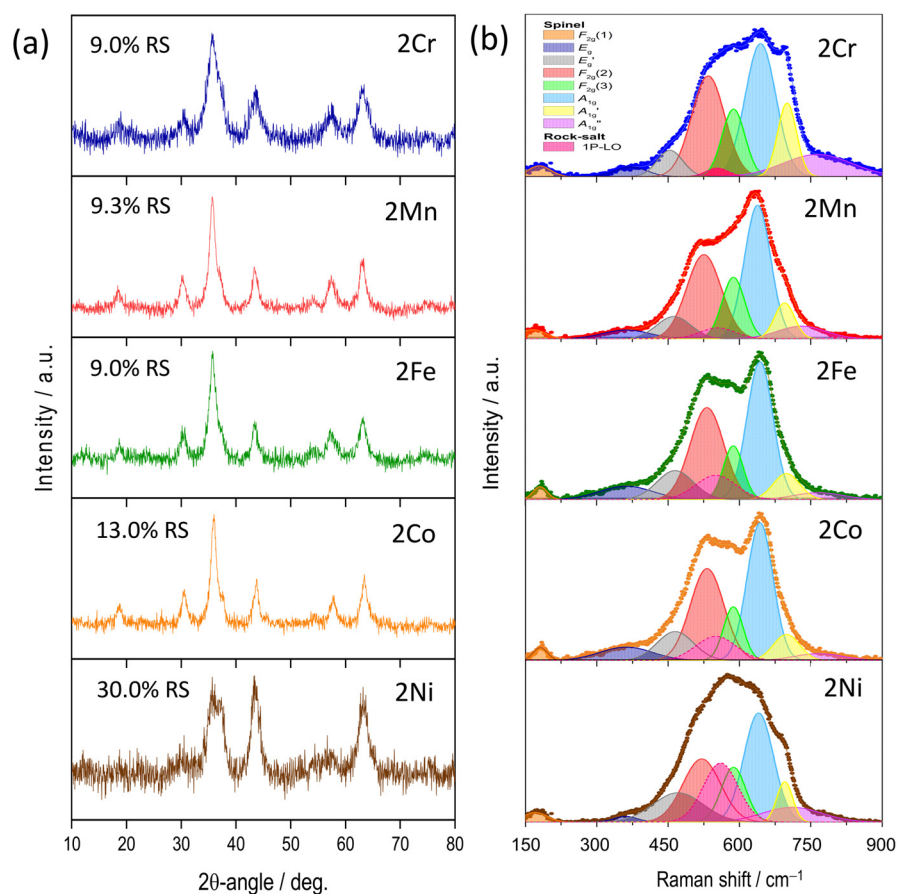


Figure 2. (a) XRD patterns. The relative amount of rock-salt (RS) impurities is reported; (b) Averaged micro-Raman spectra. Both XRD patterns and micro-Raman spectra are normalized for an easier comparison.

Measurements of Raman scattering from various random positions on each sample (not shown for brevity) prove the spatial homogeneity of all HEOs. The average micro-Raman spectra (Figure 2b) show modes typical of spinel oxides, superimposed on a weaker contribution attributable to RS impurities, confirming previously obtained results [28]. Furthermore, XPS analysis reveals the presence of oxygen vacancies (OVs) on the surface of all samples with concentration ranging from 21.6 at.% (2Cr) to 33.5 at.% (2Fe) [28].

The direct and indirect E_g values of all HEOs are determined by the Tauc plot method. For this purpose, the acquired diffuse reflectance spectra are converted into Kubelka-Munk function $F(R)$, which is proportional to the absorption coefficient and the values of $(hvF(R))^{1/n}$, with $n = 2$ (Figure 3a) and $n = 1/2$ (Figure 3b) for indirect and direct allowed transitions, respectively, are plotted as a function of hv . In both cases, E_g is given by the energy value (x-axis, eV) at the intersection point with the line tangent to the $(hvF(R))^{1/n}$ curve, in the linear sections. Since the HEOs are complex systems in which the metal cations are randomly distributed in the lattice, the co-presence of both direct and indirect transitions can be assumed. The calculated E_g values do not differ significantly from each other except for the slight increase in indirect E_g observed for the 2Cr sample. Since the particle size affects the light absorption properties and the bandgap, the nearly constant E_g values obtained are consistent with the morphological characteristics of the samples.

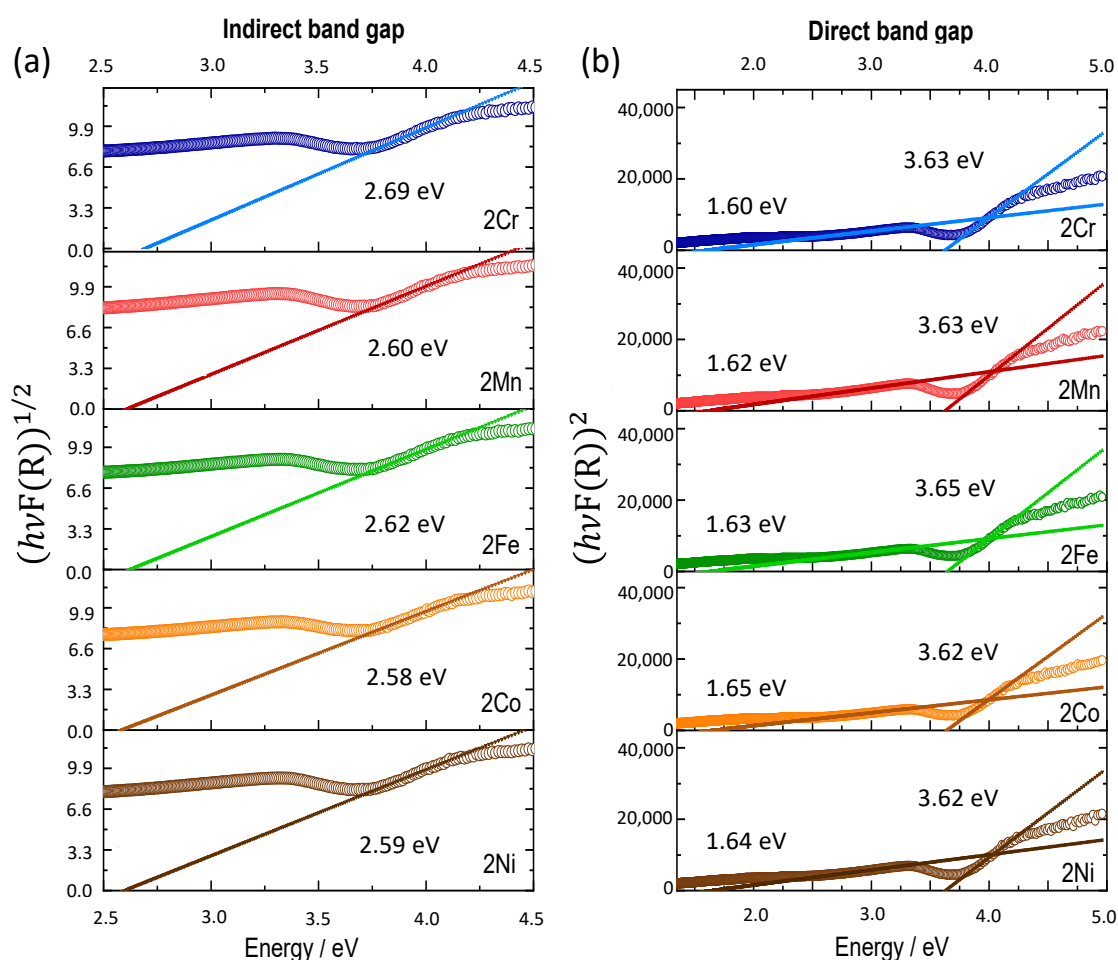


Figure 3. Tauc plot of (a) indirect and (b) direct allowed transitions of HEOs.

3.2. Photocatalytic Activity of HEOs

In order to evaluate the photocatalytic activity of HEOs in the degradation of MB under 350 nm UV irradiation at RT, the absorbance spectra in the 15 μM aqueous MB solution were measured. The spectrum of aqueous MB solution is featured by an intense absorption band, attributed to the $n\text{-}\pi^*$ transition, at 664 nm and a shoulder, originating from and 0-1 vibronic transition, at 610 nm [33]. Since the intensity of the absorbance band is proportional to the dye concentration in the aqueous solution, its degradation can be easily monitored by following the time evolution of the spectral profile, as shown in Figure 4a–c for different loads (0.30–0.96 $\text{g}\cdot\text{L}^{-1}$) of the 2Fe PC, as an example.

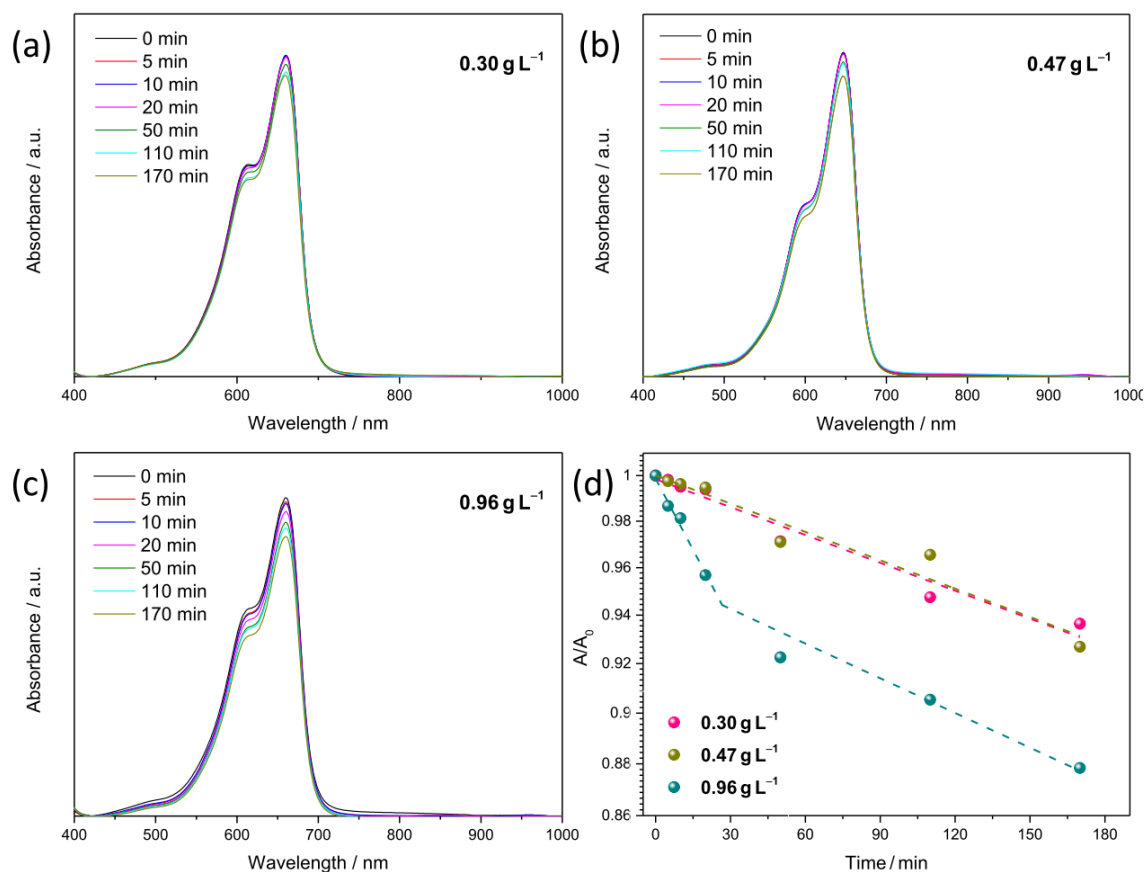


Figure 4. Time evolution of the MB absorbance spectrum for different PC loadings (a) 0.30 g·L⁻¹; (b) 0.47 g·L⁻¹ and (c) 0.96 g·L⁻¹; respectively; (d) residual MB amounts in 15 μM aqueous solution under UV radiation. The shown absorbance spectra, referring to the 2Fe PC, are normalized for a direct comparison between each other.

Different from what has been reported in the literature for HEO based on the same metal combination [34], regardless of the catalyst loading, after 170 min of UV exposure, the MB concentration in water is still high. The best result in terms of degradation is obtained with the highest PC concentration (Figure 4d). Correspondingly, after 170 min of illumination, the residual MB amount is approximately 88%, a value only slightly lower than those achieved at the lower PC concentrations (93–94%). Regardless of the presence of the PC, the kinetics of the photodegradation process can be described by a pseudo first-order law [11], as $\ln(A_t/A_0) = -k \cdot t$, where k indicates the apparent reaction rate constant. Increasing the 2Fe PC concentration, the k values obtained as the slope of the curves via a best-fit procedure are $3.99 \cdot 10^{-4} \text{ min}^{-1}$ for 0.30 g·L⁻¹ and $4.04 \cdot 10^{-4} \text{ min}^{-1}$ for 0.47 g·L⁻¹. Instead, for 0.96 g·L⁻¹, two rate constants can be distinguished, namely, $15.2 \cdot 10^{-4} \text{ min}^{-1}$, associated to an initially faster degradation process, and $3.68 \cdot 10^{-4} \text{ min}^{-1}$ that is comparable with the rate constants previously found for lower PC concentration.

As widely reported, the dye photodegradation mechanism in metal oxides [35,36], including HEOs [34], is based on the formation of hydroxyl groups (OH⁻) or hydroxyl radicals ([•]OH) and oxygen radicals (O₂^{-•}). The former species originate from the reaction between photo-generated holes in valence band and the chemisorbed water molecules, whereas O₂^{-•} radicals are generated via the trapping of the photo-generated electrons by oxygen molecules. In this mechanism, intragap states due to the lattice defects play a key role, as they reduce the recombination rate of photo-generated electron-hole pairs, thus favouring the formation of reactive radicals.

The reason for the interest in HEOs as catalysts lies in the possibility of regulating the width and position of the bandgap and generating lattice defects and deformations, thanks to their multimetallic composition, thus improving their photocatalytic activity. Actually, as shown in Figure 3, present HEOs are multigap systems, in which direct and indirect transitions in the visible spectral range coexist. In particular, for direct transitions, two E_g values are determined. 2Fe is featured by the highest OV concentration (33.5 at.%, from XPS analysis [28]) among the investigated samples. OVs are beneficial for the photocatalytic activity as they introduce donor levels into the electronic structure, suppressing the electron/hole recombination, while providing active adsorption sites for O₂ and water molecules [37,38]. Furthermore, the wavelength (340 nm, corresponding to 3.65 eV) used for catalyst photoactivation encompasses the entire energy range of transitions allowed for these materials, ensuring

the initialization of carrier photogeneration. Despite its promising structural characteristics, however, 2Fe does not exhibit satisfactory catalytic activity for MB photodegradation.

The role of H_2O_2 as PC for photodegradation is widely recognized [39]. Under UV illumination, H_2O_2 decomposes to generate $\cdot\text{OH}$, which oxidize MB molecules into MB radicals (MB^\cdot) and subsequently into intermediate products, CO_2 , and H_2O . The key step in this process is the photolytic formation of $\cdot\text{OH}$ radicals from H_2O_2 , which drive the degradation of organic molecules. Additionally, $\text{O}_2^{\cdot-}$ contribute to the MB oxidation, further promoting its conversion to CO_2 and H_2O . This process can be exploited to improve the photocatalytic activity of metal oxides, such as HEOs [34], where H_2O_2 is used as promoter for the generation of $\cdot\text{OH}$ radicals under UV illumination to increase the efficiency of the pollutant photodegradation. Hence, in the following, to compare the results obtained with present PCs with those reported in the literature, the 2Fe concentration is set at $0.47 \text{ g}\cdot\text{L}^{-1}$ and H_2O_2 is added to the MB/water solution at different dilutions. Figure 5a,b present the time evolution of the absorbance spectra observed. Figure 5c compares the degradation rate with and without H_2O_2 . The addition of H_2O_2 to the MB aqueous solution enhances the MB photodegradation. In particular, the introduction of $45 \mu\text{L}$ of H_2O_2 (30% dilution) results in a residual MB concentration of 88% at 230 min, which further decreases to 71% after 230 min when $430 \mu\text{L}$ of H_2O_2 (3% dilution) is used. Regardless of the H_2O_2 dilution, two photodegradation processes can be distinguished. The rate constants are $k_1 = 11.5 \cdot 10^{-4} \text{ min}^{-1}$ and $k_2 = 3.8 \cdot 10^{-4} \text{ min}^{-1}$ for the highest dilution, and $k_1 = 39.3 \cdot 10^{-4} \text{ min}^{-1}$ and $k_2 = 5.5 \cdot 10^{-4} \text{ min}^{-1}$ for the lowest dilution.

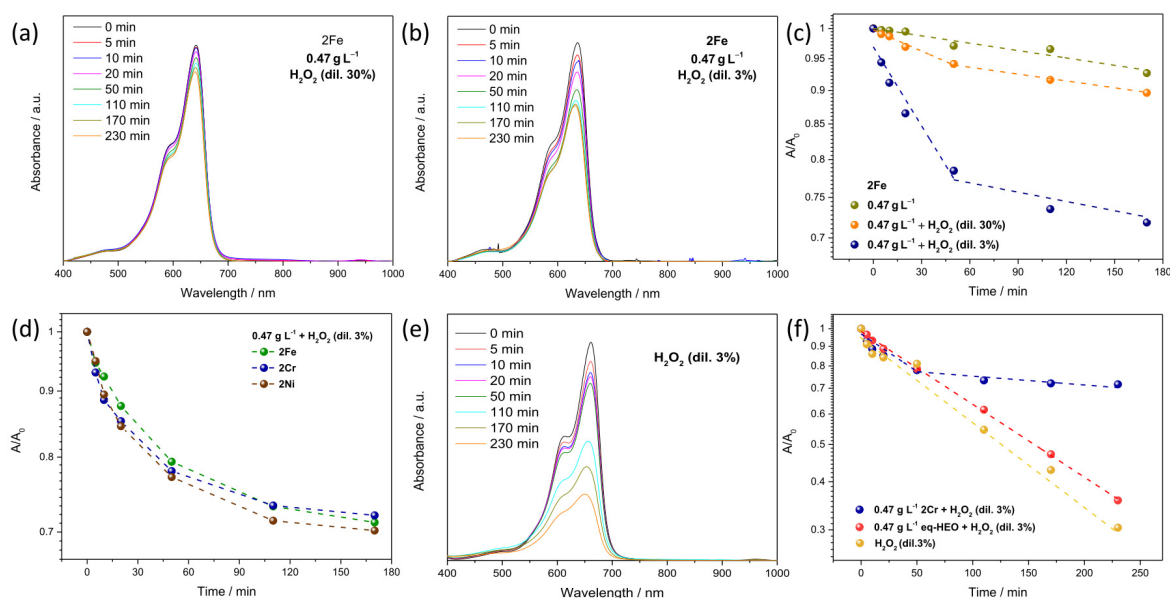


Figure 5. Time evolution of the MB absorbance spectrum, for $0.47 \text{ g}\cdot\text{L}^{-1}$ PC loading, in the presence of H_2O_2 , with (a) 30% and (b) 3% dilution. The absorbance spectra are normalized for a direct comparison between each other; (c) Degradation rate of the MB in $15 \mu\text{M}$ aqueous solution under UV radiation for $0.47 \text{ g}\cdot\text{L}^{-1}$ 2Fe PC loading with and without H_2O_2 ; (d) MB degradation rates for $0.47 \text{ g}\cdot\text{L}^{-1}$ 2Fe, 2Cr, and 2Ni PC loading and 3% diluted H_2O_2 ; (e) Time evolution of the MB absorbance spectrum in the presence of 3% diluted H_2O_2 alone; (f) Degradation rates for 3% diluted H_2O_2 alone ($k = 28.6 \cdot 10^{-4} \text{ min}^{-1}$) and for $0.47 \text{ g}\cdot\text{L}^{-1}$ 2Fe and eq-HEO PC loading and 3% diluted H_2O_2 ($k = 27.7 \cdot 10^{-4} \text{ min}^{-1}$).

In the presence of the other PCs, the use of H_2O_2 as promoter for the MB photodegradation leads to comparable performance (Figure 5d). After 230 min of reaction, the residual MB concentration is still above 70%. The non-linear trend of the degradation curve suggests the occurrence of a saturation effect, which appears to begin approximately 50 min after the onset of the photodegradation process. Since the OV concentration in these PCs ranges from 22 to 33.5 at.%, it is argued that this parameter is not the main factor governing their photocatalytic performance in MB degradation.

To understand the cause of the saturation, the photodegradation of MB obtained using $430 \mu\text{L}$ of H_2O_2 (3% dil.) alone is considered (Figure 5e). In this case, the photodegradation rate rapidly approaches zero (45% MB residue after 110 min of UV exposure), without saturating (Figure 5f). Therefore, it is supposed that the saturation effect relies with the high density of lattice defects in the PCs and, possibly, with the presence of a secondary RS oxide phase. To get a deeper insight onto the role of defects, a HEO based on the same metal combination, with similar architecture, larger grains (61 nm against 5–9 nm) and comparable OV concentration (33 at.%) [27,30] is used as

a PC for the photodegradation of MB (eq-HEO). As illustrated in a previous work [29], this sample, prepared via the same synthesis route and calcination at higher temperature (800 °C for 2 h), consists of a single pure-spinel phase. Under the same conditions, the degradation curve of eq-HEO shows a linear time dependence, with a residual amount of MB equal to 36% after 230 min of UV exposure. Nonetheless, the photodegradation of MB shows faster kinetics in the presence of H₂O₂ alone.

Kato et al. [40] have pointed out that OVs can play an ambivalent role in photocarrier dynamics, either promoting or suppressing carrier recombination. The key factor is the defect density: when defects are sparsely distributed, trapped electrons must migrate over long distances via sequential hopping and tunnelling mechanism before recombining with holes, which slows down recombination. Conversely, in the case of densely distributed defects, the probability of hopping and tunnelling processes increases and the trapped electrons can easily transfer between nearby trap states, thereby facilitating recombination.

In the investigated HEO PCs, the temperature of post-spinning thermal treatment determines both their crystalline phase and morphological features, and in turn the density and nature of lattice defects. Dangling bonds at the grain boundaries (GBs) act as traps and promote recombination processes. In eq-HEO, the higher calcination temperature leads to improved crystallinity and larger grains, thus reducing the density of GBs. On the contrary, in the other HEOs, the low calcination temperature limits the growth of grains (≤ 9 nm), resulting in a very high density of GBs and a plethora of defects easily accessible on their surface [41]. The latter situation, which favors recombination, accounts for the poor photocatalytic performance of 2X HEOs. On the contrary, the lower GB density in eq-HEO enables more efficient photocarrier separation and ultimately enhances the MB degradation efficiency. The interplay between grain size and GB defect distribution is illustrated in more details in the Supplementary Information (Figure S2).

Finally, the worse degradation efficiency of eq-HEO PC and 3% diluted H₂O₂ compared to H₂O₂ alone can be attributed to the turbidity of the solution in the presence of the catalyst, which hinders the penetration of light (Figure S3) and, consequently, reduces the photoexcitation rate.

4. Conclusions

Cr–Mn–Fe–Co–Ni-HEOs, prepared via electrospinning and calcination in air at 400 °C for 2 h, are evaluated as photocatalysts for the degradation of methylene blue in 15 μ M aqueous solution under UV irradiation. Despite their promising physicochemical properties (multigap systems consisting of densely packed ultra-small grains, with very large density of grain boundaries and copious oxygen vacancies on their surface), they exhibit poor catalytic performance. After 170 min UV exposure, with PC loadings in the 0.30–0.96 g·L⁻¹ range, the residual MB amount is still between 94 and 88%.

For a fixed PC loading (0.47 g·L⁻¹), the addition to the MB/water solution of H₂O₂ at different dilutions (30 and 3%) leads to a moderate improvement regardless of the HEO composition. After 230 min UV exposure, with 3% diluted H₂O₂ the residual MB concentration decreases to 71%. Under the same conditions, by far better results are obtained using Cr–Mn–Fe–Co–Ni-HEO calcined at higher temperature, consisting of larger grains (61 nm against 5–9 nm). This finding proves that the high density of GBs and the plethora of defects on the surface of the former PCs favor recombination, whereas the lower GB density in the latter enables more efficient photocarrier separation and ultimately enhances the MB degradation efficiency. In addition to the GB defects, the turbidity of the solution in the presence of the PC can hinder the penetration of light and, consequently, reduce the photoexcitation rate. In 2X HEOs, the small size of the PC grains boosts both causes of poor photocatalytic performance.

The presented results could be useful for the rational design of the photocatalysts. However, since 3% diluted H₂O₂, alone, is here found to be able to effectively and rapidly degrade the dye, when hydrogen peroxide is added to promote degradation, great care should be taken in assessing the real role of the catalyst.

Supplementary Materials

The additional data and information can be downloaded at: <https://media.sciltp.com/articles/others/2603021516388964/PS-25110099-SM.pdf>. Figure S1: Reflectance spectra of investigated HEOs. Figure S2: GB density as a function of size of HEO nanoparticles. Figure S3: UV-Vis absorbance spectra measured on two aqueous solutions with the same load (0.235 g L⁻¹) of 2Fe and eq-HEO PCs.

Author Contributions

C.A.: investigation, validation; Z.D.: investigation, validation; S.M.: investigation, validation; M.D.: investigation, validation, writing—original draft; S.P.: conceptualization, investigation, validation, writing—review and editing; S.S.: conceptualization, data curation, formal analysis, writing—original draft, writing—review and

editing; C.T.: investigation, validation, supervision, writing—original draft. All authors have read and agreed to the published version of the manuscript.

Funding

This research received no external funding.

Institutional Review Board Statement

Not applicable.

Informed Consent Statement

Not applicable.

Data Availability Statement

The data presented in this study are available on request from the corresponding authors.

Conflicts of Interest

The authors declare no conflict of interest.

Use of AI and AI-Assisted Technologies

No AI tools were utilized for this paper.

References

1. Khan, I.; Saeed, K.; Zekker, I.; et al. Review on Methylene Blue: Its Properties, Uses, Toxicity and Photodegradation. *Water* **2022**, *14*, 242. <https://doi.org/10.3390/w14020242>.
2. Shah, D.I.; Santani, D.D.; Goswami, S.S. A Novel Use of Methylene Blue as a Pharmacological Tool. *J. Pharmacol. Toxicol. Methods* **2006**, *54*, 273–277. <https://doi.org/10.1016/j.vascn.2005.12.003>.
3. Kathi, S.; El Din Mahmoud, A. Trends in Effective Removal of Emerging Contaminants from Wastewater: A Comprehensive Review. *Desal. Water Treat.* **2024**, *317*, 100258. <https://doi.org/10.1016/j.dwt.2024.100258>.
4. Siong, V.L.E.; Lee, K.M.; Juan, J.C.; et al. Removal of Methylene Blue Dye by Solvothermally Reduced Graphene Oxide: A Metal-Free Adsorption and Photodegradation Method. *RSC Adv.* **2019**, *9*, 37686–37695. <https://doi.org/10.1039/C9RA05793E>.
5. Jiang, G.; Zheng, X.; Wang, Y.; et al. Photo-Degradation of Methylene Blue by Multi-Walled Carbon Nanotubes/TiO₂ Composites. *Powder Technol.* **2011**, *207*, 465–469. <https://doi.org/10.1016/j.powtec.2010.11.029>.
6. Berehe, B.A.; Desalew, A.A.; Derbe, G.W.; et al. Enhanced Photocatalytic Degradation of Methylene Blue Dye via Valorization of a Polyethylene Terephthalate Plastic Waste-Derived Metal–Organic Framework-Based ZnO@Co-BDC Composite Catalyst. *Nanoscale Adv.* **2025**, *7*, 3834–3845. <https://doi.org/10.1039/D4NA01071J>.
7. Shah, S.S.; Ramos, B.; Otubo, L.; et al. Deep Removal and Photodegradation of Methylene Blue Dye Using Superabsorbent Polymer Hydrogel Composite with Activated Charcoal and TiO₂ Nanoparticles. *ACS Omega* **2025**, *10*, 26441–26457. <https://doi.org/10.1021/acsomega.4c11428>.
8. Nasrollahpour, A.; Moradi, S.E. Photochemical Degradation of Methylene Blue by Metal Oxide-Supported Activated Carbon Photocatalyst. *Desal. Water Treat.* **2016**, *57*, 8854–8862. <https://doi.org/10.1080/19443994.2015.1035675>.
9. Chatterjee, D.; Dasgupta, S. Visible Light Induced Photocatalytic Degradation of Organic Pollutants. *J. Photochem. Photobiol. C* **2005**, *6*, 186–205. <https://doi.org/10.1016/j.jphotochemrev.2005.09.001>.
10. Petrovičová, B.; Dahrouch, Z.; Triolo, C.; et al. Photocatalytic Degradation of Methylene Blue Dye by Electrospun Binary and Ternary Zinc and Titanium Oxide Nanofibers. *Appl. Sci.* **2021**, *11*, 9720. <https://doi.org/10.3390/app11209720>.
11. Pantò, F.; Dahrouch, Z.; Saha, A.; et al. Photocatalytic Degradation of Methylene Blue Dye by Porous Zinc Oxide Nanofibers Prepared via Electrospinning: When Defects Become Merits. *Appl. Surf. Sci.* **2021**, *557*, 149830. <https://doi.org/10.1016/j.apsusc.2021.149830>.
12. Guillén, C. Determination of the Band Gap Energy of SnO₂ and ZnO Thin Films with Different Crystalline Qualities and Doping Levels. *Electron. Mater.* **2025**, *6*, 3. <https://doi.org/10.3390/electronicmat6010003>.
13. Khattab, E.-S.R.; Abd El Rehim, S.S.; Hassan, W.M.I.; et al. Band Structure Engineering and Optical Properties of Pristine and Doped Monoclinic Zirconia (*m*-ZrO₂): Density Functional Theory Theoretical Prospective. *ACS Omega* **2021**, *6*, 30061–30068. <https://doi.org/10.1021/acsomega.1c04756>.

14. Wetchakun, N.; Chainet, S.; Phanichphant, S.; et al. Efficient Photocatalytic Degradation of Methylene Blue over BiVO₄/TiO₂ Nanocomposites. *Ceram. Int.* **2015**, *41*, 5999–6004. <https://doi.org/10.1016/j.ceramint.2015.01.040>.
15. Giroto, G.Z.; Thill, A.S.; Matte, L.P.; et al. Ni/SrTiO₃ Nanoparticles for Photodegradation of Methylene Blue. *ACS Appl. Nano Mater.* **2022**, *5*, 13295–13307. <https://doi.org/10.1021/acsanm.2c03007>.
16. Tahir, M.N. Synthesis of Hierarchically Organized α -Fe₂O₃ Nanostructures for the Photocatalytic Degradation of Methylene Blue. *Emergent Mater.* **2020**, *3*, 605–612. <https://doi.org/10.1007/s42247-020-00127-9>.
17. DePuccio, D.P.; Botella, P.; O'Rourke, B.; et al. Degradation of Methylene Blue Using Porous WO₃, SiO₂-WO₃, and Their Au-Loaded Analogs: Adsorption and Photocatalytic Studies. *ACS Appl. Mater. Interfaces* **2015**, *7*, 1987–1996. <https://doi.org/10.1021/am507806a>.
18. Bai, S.; Zhang, N.; Gao, C.; et al. Defect Engineering in Photocatalytic Materials. *Nano Energy* **2018**, *53*, 296–336. <https://doi.org/10.1016/j.nanoen.2018.08.058>.
19. Senthamizhan, A.; Balusamy, B.; Aytac, Z.; et al. Grain Boundary Engineering in Electrospun ZnO Nanostructures as Promising Photocatalysts. *CrystEngComm* **2016**, *18*, 6341–6351. <https://doi.org/10.1039/C6CE00693K>.
20. Sarkar, A.; Wang, Q.; Schiele, A.; et al. High-Entropy Oxides: Fundamental Aspects and Electrochemical Properties. *Adv. Mater.* **2019**, *31*, 1806236. <https://doi.org/10.1002/adma.201806236>.
21. Sun, Y.; Wu, T.; Bao, Z.; et al. Defect Engineering of Ceria Nanocrystals for Enhanced Catalysis via a High-Entropy Oxide Strategy. *ACS Cent. Sci.* **2022**, *8*, 1081–1090. <https://doi.org/10.1021/acscentsci.2c00340>.
22. Jia, D.; Chigan, T.; Li, X.; et al. Photocatalytic Degradation Performance for High-Entropy Oxide (La_{0.2}Ce_{0.2}Gd_{0.2}Zr_{0.2}Fe_x)O₂ Enriched with Defects. *J. Alloys Compd.* **2024**, *982*, 173808. <https://doi.org/10.1016/j.jallcom.2024.173808>.
23. Pradhan, S.; Barick, K.C.; Anuraag, N.S.; et al. Development of Ferrimagnetic (Mn_{0.6}Cr_{0.6}Co_{0.6}Fe_{0.6}Al_{0.6})O₄ High Entropy Oxide for Photo-Fenton Degradation of Organic Dye. *Appl. Surf. Sci.* **2025**, *688*, 162343. <https://doi.org/10.1016/j.apsusc.2025.162343>.
24. Zhang, F.; Zhou, W.; Zhang, Y.; et al. Spectroscopic Analyses and Photocatalytic Properties of Transition Group Metal Oxide Films with Different Entropy Values. *Mater. Sci. Semicond. Process.* **2024**, *169*, 107928. <https://doi.org/10.1016/j.mssp.2023.107928>.
25. Du, M.; Liu, S.; Ge, Y.; et al. Preparation and Effect of Grain Size on the Thermal Stability, Phase Transition, Mechanical Property, and Photocatalytic Property of Pyrochlore (La_{0.2}Nd_{0.2}Sm_{0.2}Gd_{0.2}Y_{0.2})₂Zr₂O₇ High-Entropy Oxide. *Ceram. Int.* **2022**, *48*, 20667–20674. <https://doi.org/10.1016/j.ceramint.2022.04.046>.
26. Triolo, C.; Moulace, K.; Ponti, A.; et al. Spinel-Structured High-Entropy Oxide Nanofibers as Electrocatalysts for Oxygen Evolution in Alkaline Solution: Effect of Metal Combination and Calcination Temperature. *Adv. Funct. Mater.* **2024**, *34*, 2306375. <https://doi.org/10.1002/adfm.202306375>.
27. Vezzù, K.; Triolo, C.; Moulace, K.; et al. Interplay Between Calcination Temperature and Alkaline Oxygen Evolution of Electrospun High-Entropy (Cr_{1/5}Mn_{1/5}Fe_{1/5}Co_{1/5}Ni_{1/5})₃O₄ Nanofibers. *Small* **2025**, *21*, 2408319. <https://doi.org/10.1002/smll.202408319>.
28. Triolo, C.; Moulace, K.; Bellato, F.; et al. Interplay between Alkaline Water Oxidation Temperature, Composition and Performance of Electrospun High-Entropy Non-Equimolar (Cr,Mn,Fe,Co,Ni) Oxide Electrocatalysts. *J. Power Sources* **2025**, *654*, 237887. <https://doi.org/10.1016/j.jpowsour.2025.237887>.
29. Patriarchi, A.; Triolo, C.; Minnetti, L.; et al. Evaluation of High-Entropy (Cr, Mn, Fe, Co, Ni)-Oxide Nanofibers and Nanoparticles as Passive Fillers for Solid Composite Electrolytes. *Electrochim. Acta* **2025**, *512*, 145425. <https://doi.org/10.1016/j.electacta.2024.145425>.
30. Triolo, C.; Patriarchi, A.; Darjazi, H.; et al. Electrospun Spinel-Structured High-Entropy Oxide Nanofibers as Fillers for Solid Polymer Electrolytes: The Pivotal Role of Oxygen Vacancies. *IL Nuovo Cimento C* **2025**, *48*, 246. <https://doi.org/10.1393/ncc/i2025-25246-3>.
31. Altomare, A.; Cuocci, C.; Giacobazzo, C.; et al. QUALX: A Computer Program for Qualitative Analysis Using Powder Diffraction Data. *J. Appl. Crystallogr.* **2008**, *41*, 815–817. <https://doi.org/10.1107/S0021889808016956>.
32. Altomare, A.; Corriero, N.; Cuocci, C.; et al. QUALX2.0: A Qualitative Phase Analysis Software Using the Freely Available Database POW_COD. *J. Appl. Crystallogr.* **2015**, *48*, 598–603. <https://doi.org/10.1107/S1600576715002319>.
33. Heger, D.; Jirkovský, J.; Klán, P. Aggregation of Methylene Blue in Frozen Aqueous Solutions Studied by Absorption Spectroscopy. *J. Phys. Chem. A* **2005**, *109*, 6702–6709. <https://doi.org/10.1021/jp050439j>.
34. Sur, S.; Vekariya, N.; Jha, S.K.; et al. High Entropy Spinel Oxide for Natural Sunlight-Driven Photocatalytic Degradation of Methylene Blue: A Sustainable Water Remediation Process. *Results Surf. Interfaces* **2025**, *19*, 100549. <https://doi.org/10.1016/j.rsufi.2025.100549>.
35. Kalaycıoğlu, Z.; Özüğür Uysal, B.; Pekcan, Ö.; et al. Efficient Photocatalytic Degradation of Methylene Blue Dye from Aqueous Solution with Cerium Oxide Nanoparticles and Graphene Oxide-Doped Polyacrylamide. *ACS Omega* **2023**, *8*, 13004–13015. <https://doi.org/10.1021/acsomega.3c00198>.

36. Talebian, N.; Nilforoushan, M.R. Comparative Study of the Structural, Optical and Photocatalytic Properties of Semiconductor Metal Oxides toward Degradation of Methylene Blue. *Thin Solid Films* **2010**, *518*, 2210–2215. <https://doi.org/10.1016/j.tsf.2009.07.135>.
37. Zafar, Z.; Yi, S.; Li, J.; et al. Recent Development in Defects Engineered Photocatalysts: An Overview of the Experimental and Theoretical Strategies. *Energy Environ. Mater.* **2022**, *5*, 68–114. <https://doi.org/10.1002/eem2.12171>.
38. Tsubota, H.; Jitianu, A.; Kawamura, G. Recent Advances in High-Entropy Oxides for Photocatalytic Applications. *ACS Mater. Lett.* **2025**, *7*, 1042–1056. <https://doi.org/10.1021/acsmaterialslett.4c02323>.
39. Ali, M.A.; Maafa, I.M.; Qudsieh, I.Y. Photodegradation of Methylene Blue Using a UV/H₂O₂ Irradiation System. *Water* **2024**, *16*, 453. <https://doi.org/10.3390/w16030453>.
40. Kato, K.; Uemura, Y.; Asakura, K.; et al. Role of Oxygen Vacancy in the Photocarrier Dynamics of WO₃ Photocatalysts: The Case of Recombination Centers. *J. Phys. Chem. C* **2022**, *126*, 9257–9263. <https://doi.org/10.1021/acs.jpcc.2c01662>.
41. Rezaei, M.; Nezamzadeh-Ejhieh, A.; Massah, A.R. A Comprehensive Review on the Boosted Effects of Anion Vacancy in the Heterogeneous Photocatalytic Degradation, Part II: Focus on Oxygen Vacancy. *ACS Omega* **2024**, *9*, 6093–6127. <https://doi.org/10.1021/acsomega.3c07560>.